Nanoscale

Plasmonic Nanorod Probes' Journey inside Plant Cells for In Vivo SERS Sensing and Multimodal Imaging

Journal:	*Nanoscale*
Manuscript ID	NR-ART-11-2022-006235.R2
Article Type:	Paper
Date Submitted by the Author:	06-Mar-2023
Complete List of Authors:	Cupil Garcia, Vanessa; Duke University, Fitzpatrick Institute for Photonics Li, Joy; Duke University, Fitzpatrick Institute for Photonics Stephen, Stephen; Duke University, Fitzpatrick Institute of Photonics Odion, Ren; Duke University Strobbia, Pietro; University of Cincinnati, Menozzi, Luca; Duke University, Fitzpatrick Institute for Photonics Ma, Chenshuo; Duke University, Fitzpatrick Institute for Photonics Hu, Jianhong; Duke University, Department of Biology Zentella, Rodolfo; Duke University, Department of Biology Boyanov, Maxim; Argonne National Laboratory, Biosciences Division Finfrock, Y. Zou; cCLS@APS sector 20, Advanced Photon Source, Argonne National Laboratory Gursoy, Doga; Northwestern University, Department of Electrical Engineering and Computer Science Douglas , Deirdre; Argonne National Laboratory, Biosciences Division Yao, Junjie; Duke University, Sun, Tai-Ping; Duke University, Department of Biology Kemner, Ken; Argonne National Lab, BioSciences Tuan, Vo-Dinh; Duke University,

ARTICLE

Plasmonic Nanorod Probes' Journey inside Plant Cells for *In vivo* SERS Sensing and Multimodal Imaging

Received 00th January 20xx,
Accepted 00th January 20xx

DOI: 10.1039/x0xx00000x

Vanessa Cupil-Garcia[a,b], Joy Q Li[a,c], Stephen J Norton[a], Ren A Odion[a,c], Pietro Strobbia[a,c,1], Luca Menozzi[a,c], Chenshuo Ma[a,c], Jianhong Hu[d], Rodolfo Zentella[d,2,3], Maxim I. Boyanov[e,f], Y. Zou Finfrock[g], Doga Gursoy[g,h], Deirdre Sholto Douglas[f,4], Junjie Yao[a,c], Tai-Ping Sun[d], Kenneth M. Kemner[f], and Tuan-Vo-Dinh[a,b,c] (*)

Nanoparticle-based platforms are gaining strong interest in plant biology and bioenergy research to monitor and control biological processes in whole plants. However, in vivo monitoring of biomolecules using nanoparticles inside plant cells remains challenging due to the impenetrability of the plant cell wall to nanoparticles beyond the exclusion limits (5-20 nm). To overcome this physical barrier, we have designed unique bimetallic silver-coated gold nanorods (AuNR@Ag) capable of entering plant cells, while conserving key plasmonic properties in the near-infrared (NIR). To demonstrate cellular internalization and tracking of the nanorods inside plant tissue, we used a comprehensive multimodal imaging approach that included transmission electron microscopy (TEM), confocal fluorescence microscopy, two-photon luminescence (TPL), X-ray fluorescence microscopy (XRF), and photoacoustics imaging (PAI). We successfully acquired SERS signals of nanorods in vivo inside plant cells of tobacco leaves. On the same leaf samples, we applied orthogonal imaging methods, TPL and PAI techniques for in vivo imaging of the nanorods. This study first demonstrates the intracellular internalization of AuNR@Ag inside whole plant systems for in vivo SERS analysis in tobacco cells. This work demonstrates the potential of this nanoplatform as a new nanotool for intracellular in vivo biosensing for plant biology.

1. Introduction

Probing intracellular pathways and biomarkers in plants is important in bioengineering crops for bioenergy, biofuel, and agricultural purposes. There is a strong need to increase bioenergy production considering the rising global demand for energy and that biomass generated energy contributes to 50% of renewable energy production.[1] Biofuels can be produced more efficiently by genetically transforming plants to overexpress or supress expression of certain biomarkers in pathways such as the flowering or lignin producing pathways.[2, 3] Standard procedures for examining plant genetic markers such as PCR are not able to acquire information in real time with adequate temporal or spatial resolution and are furthermore destructive to the plant tissue.[4] To label these pathways for monitoring at the cellular level requires entering plant cells which is challenged by the physical barriers of the plant cell wall.

Genetic transformation, biomolecule monitoring, and nanoparticle incorporation into cells is regulated by diameter and size exclusion limits of plant cell pores and tissues.[5-9] The porosity of the plant cell wall (5 to 20 nm) is a major parameter limiting nanoparticle uptake.[5, 9] Currently, limited methods exist for enabling direct entry into plant cells to measure biomarkers, enable genetic manipulation, or probe biochemical pathways. Electroporation and biolistic particle delivery use mechanical force that causes damages to the plant tissue and leads to unstable gene expression. Agrobacterium-mediated gene expression also faces challenges due to random DNA integration and can only be applied to a narrow range of hosts and tissues.[10] The intrinsic challenges of these techniques highlight the critical need for new methods of directly entering plant cells to achieve monitoring of biomarkers and biochemical pathways. Insight into these fields is in high demand to meet increasing global bioenergy needs.

Nanomaterials have distinct and unique properties differing from the bulk material, making them biocompatible and versatile options for applications in plant science. Nanoparticles open a new avenue for

[a.] *Fitzpatrick Institute for Photonics, Durham, NC 27706, USA*
[b.] *Department of Chemistry, Duke University, Durham, NC 27706, USA*
[c.] *Department of Biomedical Engineering, Duke University, Durham, NC 27706, USA*
[d.] *Department of Biology, Duke University, Durham, NC 27706, USA*
[e.] *Bulgarian Academy of Sciences, Institute of Chemical Engineering, Sofia 1113, Bulgaria*
[f.] *Biosciences Division, Argonne National Laboratory, Argonne, IL 60439, USA*
[g.] *X-ray Science Division, Advanced Photon Source, Argonne National Laboratory, Lemont, IL 60439, USA*
[h.] *Department of Electrical Engineering and Computer Science, Northwestern University, Evanston, IL 60208, USA*
† Electronic Supplementary Information (ESI) available: [details of any supplementary information available should be included here]. See DOI: 10.1039/x0xx00000x

intracellular sensing. Currently, there are numerous studies documenting the use and uptake of nanoparticles for therapy, transport, and monitoring of biomarkers such as small molecules, DNA, siRNA, proteins, and miRNA, as well as their effects in mammalian and pathogen cells.[11-26] However, research on nanoparticle integration into plants is nascent and has not been studied as extensively. Current studies have nonetheless yielded crucial information about nanoparticle uptake.[27-34] Notably, recent reports of carbon nanotubes with dimensions smaller than the plant cell wall exclusion limit have demonstrated the ability to enter plant cells and change gene expression.[7, 35] There have also been studies examining the biolistic transport of gold nanospheres, as well as gold nanorods delivered into plant tissues combined with large 0.6 µm gold nanoparticles; nevertheless, biolistic infiltration is a damaging technique to plant tissue and other passive techniques have been explored.[36-39] Recently, gold nanoclusters, spheres, and nanorods have been used for gene knockdown purposes, and intracellular internalization of gold nanorods is likely due to endocytosis.[40, 41] However, the field application of plasmonic nanosensing in plants has not been thoroughly explored, and it is evident that there is a lack of plasmonic and bimetallic nanosensors that can infiltrate plant cells and track gene expression and biomarkers in vivo. To date, the intracellular delivery and use of plasmonic bimetallic nanorods for in vivo biosensing inside plant cells has not been reported.

Collective oscillations of conduction electrons on metallic gold and silver nanoparticles produce localized surface plasmons, which induce enhanced local electromagnetic fields, leading to a strong surface-enhanced Raman scattering (SERS) effect.[42-46] The SERS effect can increase Raman signals by 10^7-10^{10}-fold, and the production of sharp Raman peaks from molecules facilitate its use for multiplex biochemical analyses in a wide variety of applications.[47, 48] Silver coating of particles has also been shown to increase SERS effects by an order of magnitude compared to their gold counterparts and have not been studied in plant tissue demonstrating the need for silver-coated plasmonic plant cell penetrating nanosensors.[49] Over three decades, our laboratory has been developing different plasmonics-active platforms such as nanowaves, nanospheres, and nanostars for many applications ranging from SERS chemical sensing to biomedical diagnostics and therapy.[50-55] More recently, we used silver-coated gold nanostars decorated with biosensing probes to monitor microRNAs in the interlamellar spaces of *Arabidopsis thaliana* leaves.[56, 57] Cellular uptake in plants has been demonstrated in published work[41], and in separate works, SERS-based nanoprobes have been used in plants with nanoparticles that accumulate in between cells.[58] However, in vivo monitoring of nanoparticles while maintaining strong plasmonic properties inside of plant cells still remains a great challenge because the plant cell wall is impenetrable to nanoparticles beyond the exclusion size limits (5-20 nm).

Before agriculturally relevant in vivo biosensing of biomarkers can be achieved, plasmonic particles, such as silver-coated nanoparticles need to enter plant cells. To this end, we investigated a new and unique nanoplatform—silver-coated gold nanorods with enhanced intracellular uptake and sensing capabilities. We studied the intracellular uptake of these nanosystems into plant cells and applied them as sensitive probes due their important properties: strong SERS enhancing capabilities and unique shape, where one dimension (13 nm) is under the plant cell wall size exclusion limit, facilitating entry of the nanomaterial in plant cells.[35, 59] We successfully achieved intracellular infiltration using an extensive multimodal validation approach consisting of transmission electron microscopy (TEM), fluorescence confocal imaging, and synchrotron x-ray fluorescence (XRF) imaging. Because nanoprobe entry into the leaf is not spatially homogenous, accuracy of quantitative analysis and probe mapping within the leaf will require normalizing SERS intensity of probes to the number of infiltrated probes at that spatial location. The combination of these techniques permits normalization of nanorod concentrations per pixel from gold amounts to determine SERS signal per nanorod. This information (i.e., particles per cell) is key for signal normalization to achieve quantitative SERS sensing. Thus, we investigated two-photon luminescence (TPL) and X-ray fluorescence imaging in plant leaves. In this study, we also demonstrated the first application of the bimetallic AuNR@Ag for photoacoustic imaging (PAI). We demonstrated that silver-coated gold nanorods can be used as efficient contrast agents for photoacoustic, SERS, and TPL imaging. The spatial and temporal resolution is conserved in the studies for the proper examination of intracellular biochemical pathways, in contrast with the current procedures that require sample extraction (e.g., PCR or chromatography). Our data demonstrate the first instance of plasmonic nanosensors accumulating inside of tobacco plant cells and generating SERS signal in vivo, which lays the foundation to meet the dire need for intracellular biosensing in plant biology research.

2. Results and discussion

2.1 Synthesis and Characterization of the Silver-coated Nanorods

The AuNR@Ag were synthesized using commercially available gold nanorod precursors. The precursors were silver-coated using silver nitrate followed by ascorbic acid. The product was blue-shifted in absorbance to 685 nm from the precursors that absorbed at 820 nm as shown in Fig. S1. This blue-shift and color change from brown to green is indicative of the silver coating.[60] Moreover, TEM images in Fig. 1A illustrate the silver coating on the

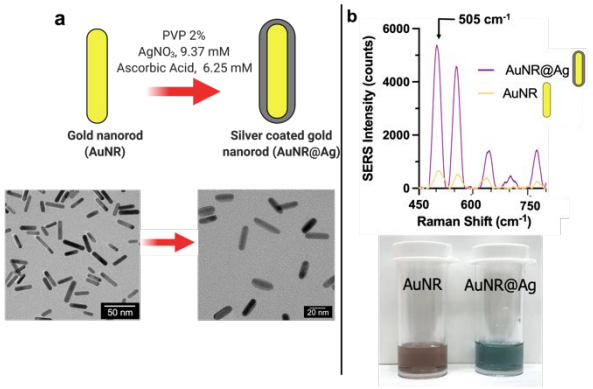

Fig 1. (a) Schematic and transmission electron microscopy images of nanorods before and after silver coating. (b) SERS spectra of nanoparticles coated with a cyanine 7 dye at the characteristic peaks (505 & 558 cm^{-1}) and the visible color change from brown to green after synthesis.

nanorods as the lighter gray layer observed surrounding the denser gold, which can be observed as the dark core. The TEM images agree with previous experimental work involving silver coating of larger gold nanorods.[60] Following silver coating, the width of the nanorods changes from 5 nm to 13 nm on average, which is favorable for plant cell infiltration, since it is smaller than the 5-20 nm plant cell wall exclusion limit of the plant cell wall pores (Table S1, Fig. S2 & S3). The zeta potential of our the AuNR@Ag was -38.03 mV and is favorable for entry into plants, in accordance with previous models predicting uptake of particles below ~20 nm and with very negative or positive zeta potentials(above ~+30 mV or below ~–30 mV).[35] Compared to AuNR, the SERS enhancement of AuNR@Ag seen in Fig. 1B and Table S2 increased at the characteristic peaks of the Raman active dye Cy7 (505 & 558 cm^{-1}), indicating that the silver coating is necessary to increase the plasmonic SERS detection capabilities of the nanosystem compared to the gold nanorod.

2.2 Delivery and Detection of Nanorods into Plant Cells

2.21 Subcellular Localization of Nanorods in Plant Cells by TEM

We first infiltrated AuNR@Ag into leaves of tobacco plants using the needleless injection procedure discussed in the methods. TEM imaging was performed to precisely examine the subcellular location of AuNR@Ag in the infiltrated leaf tissue (Fig. 2 & Fig. S4). Supplementary schematic 1 illustrates the experimental workflow for delivering and localizing AuNR@Ag inside of tobacco plants. It is evident that the AuNR@Ag nanorods were present near the chloroplasts. Fig. S5 provides additional TEM images showing that the AuNR@Ag are both inside of tobacco leaf cells and in the intercellular spaces between cells. These results confirm the ability of the plasmonic AuNR@Ag to penetrate the cell wall and accumulate inside the plant cells. The ability to locate these nanomaterials inside of cells suggest that they are ideal as a model platform for tracking intracellular processing within the plant architecture. In consideration of the limitations in

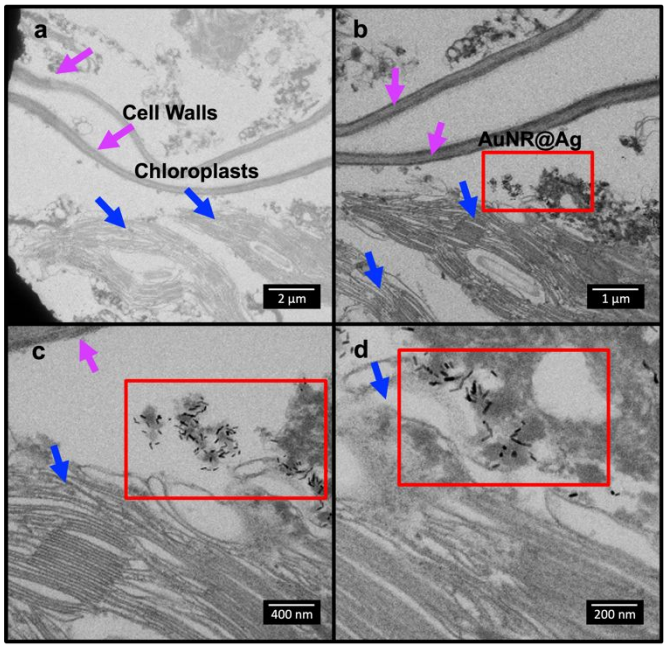

Fig. 2. Transmission electron microscopy images of AuNR@Ag inside tobacco cells. Purple arrows indicate the cell walls, and the blue arrows highlight the location of the chloroplasts which are inside of the cells. (b)-(d) are higher magnification images.

tissue processing for TEM imaging, we further studied the uptake of the AuNR@Ag inside of intact plant cells using confocal imaging and XRF imaging.

2.22 Co-localization of AuNR@Ag and GFP in the Cytoplasm by Confocal Imaging

To further examine the distribution of AuNR@Ag inside of intact plant cells, we performed confocal microscopy, since it is a well described and applied method to confirm particle uptake in plant cells.[35, 40] We infiltrated Cyanine 3 (Cy3)-labelled AuNR@Ag into tobacco leaves, which expressed GFP in the cytoplasm and nucleus. The Cy3 dye permits visualization of the AuNR@Ag outside the GFP window and the autofluorescence of plant tissue. Fig. 3 displays representative results from confocal fluorescence microscopy showing co-localization of AuNR@Ag and GFP in the cytoplasm. The tobacco plants were transformed to transiently express GFP in the leaf cells using agrobacterium containing the p35S-HA-GFP plasmid. The GFP signal is displayed as the green signal in leaf pavement cells in Fig. 3B. Pavement cells display an irregular jig-saw puzzle shape as the surface cells of the leaf, and the cytoplasm is pushed towards the boundary of the cell due to the presence of the large vacuoles; therefore, the GFP cytoplasm signal appears as the thin line with black space (vacuole) in between.[61] The transformed GFP tobacco plants were treated with the AuNR@Ag-Cy3.

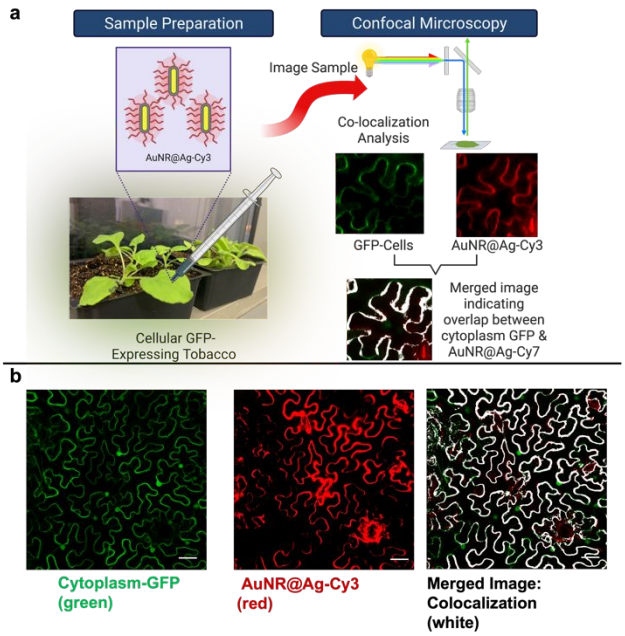

Fig. 3. (a) Representative confocal fluorescence microscopy schematic of Cy3-labelled AuNR@Ag infiltrated into tobacco plants expressing GFP fluorophore in the cytoplasm. The Cy3 channel represents the Cy3-labelled nanoparticles. The red lines on the AuNR@Ag represents the Cy3 dye functionalized on the particle. (b) Cytoplasm GFP from the GFP modified tobacco plant (green signal), AuNR@Ag-Cy3 inside of the cytoplasm of surface pavement cells (red signal), and merged image use to determine presence of the AuNR@Ag-Cy3 inside of cells (white). A 488 nm laser was used to excite the GFP channel, and a 561 nm was used to excite the Cy3 dye channel.

The AuNR@Ag-Cy3 are displayed by the red signal where they accumulate inside the plant tissue. The AuNR@Ag show effective co-localization between the intracellular GFP in the cytoplasm of pavement cells and Cy3 from the labelled AuNR@Ag with an average colocalization fraction of 0.704 ±0.0068. These results demonstrate the AuNR@Ag have a high degree of cellular penetration into the leaf cells due to one of their dimensions being smaller than the plant cell wall exclusion limit. The AuNR@Ag-Cy3 signal is clearly located in the cytoplasm. The colocalization of cytoplasm GFP signal in pavement cells with the Cy3-labeled AuNR@Ag signal provides additional experimental evidence that these plasmonic nanoparticles efficiently enter plant cells, enabling the potential for biochemical sensing inside the plant cell.

These data underscore the opportunities afforded by the AuNR@Ag entering plant cells to provide insight of cellular processes through sensing and imaging. Such data are hard to obtain with sufficient temporal and spatial resolution using traditional methods such as PCR detection of RNAs. Infiltration of cells with AuNR@Ag provides a route to better understand cell dynamics through real time in vivo imaging. Moreover, TEM and confocal fluorescence imaging demonstrate the comprehensive characterization of the AuNR@Ag inside of cells.

2.23 XRF 2D Imaging of Leaf Treated with Silver-coated Gold Nanorods

2D XRF analysis can be used for quantitative analysis of nanoparticle content in a sample [60, 61] , as XRF can directly measure gold content; these measurements have been employed in past work to normalize nanosensor response in plant tissue.[56] Samples were also analyzed using confocal XRF imaging (section 2.24). Fig. S6 compares an optical transmission microscope image of the leaf (as mounted on the X-ray stage between Kapton film) to the 2D XRF maps (14 micron spatial resolution, see Experimental section for more details) from some elements in the sample. The XRF elemental 2D maps show that the distributions of Fe, Mn, and Zn provide a good indication of leaf morphology. The Ca map also mimics the morphology, but there is also interfering Ca signal outside the leaf due to Ca-phosphate precipitates in the Kapton film. The Au map provides further confirmation that the gold particles have accumulated inside the leaf, with slightly more Au signal in the middle of the leaf. The blue rectangle drawn on the optical image delineates the area chosen for the higher resolution XRF images discussed below.

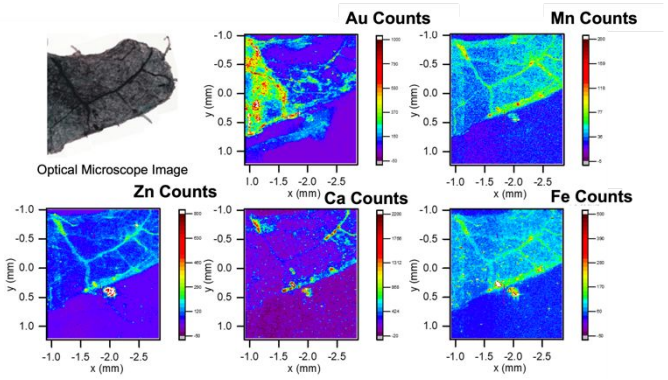

Fig. 4. Finer scale XRF images of various elements found inside the leaf and the gold from the AuNR@Ag. The dark vertical segments near x = -1.8mm are due to equipment artifacts generated during the shorter time scan.

The finer scale XRF and optical transmission microscopy images of a tobacco leaf (Fig. 4) indicate that Ca, Mn, Fe, and Zn concentrations are increased where the veins and midribs are, as well as near the edge of the leaf and, thus, enable visualization of these structures. Distributions of these elements can enable identification of cells and larger morphologies within biological samples.[62] An Fe-rich precipitate is observed outside of the leaf near (-2.0 mm, 0.5 mm). The Au signal is mostly present to the left of the vertical channel in the leaf, but also concentrates in the midribs and veins on the right side of the image as delineated by the Ca, Mn, Fe, and Zn XRF images. No discernible shape of the leaf was present in the P, S, and Cl maps (likely due to absorption of these low-energy x-rays in the ambient atmosphere).

Several locations on the Au XRF map were selected to collect the full multi-channel analyzer (MCA) spectra above

and below the Au edge, to verify the presence of Au, and to test for correlations with other elements. The probe locations are indicated on the Au map (Fig. S7), and the MCA spectra are plotted to the left. The amount of Au accumulation could not be correlated with the other elements detected at these locations. Thus, the differences between the spectra below and above the Au edge prove the presence of Au. The MCA spectrum from the precipitate near the leaf (location #3) shows elevated concentrations of Re, an assignment based on the correlation between the amplitudes of the Mα (~2000eV) and Lα (~8500eV) peaks. Because the Lα line of Re overlaps with the Kα line of Zn, it is possible that some of the amplitude observed in the Zn maps of the leaf is due to Re.

2.24 XRF Confocal Imaging of Silver-coated Gold Nanorods Infiltrated into Leaves

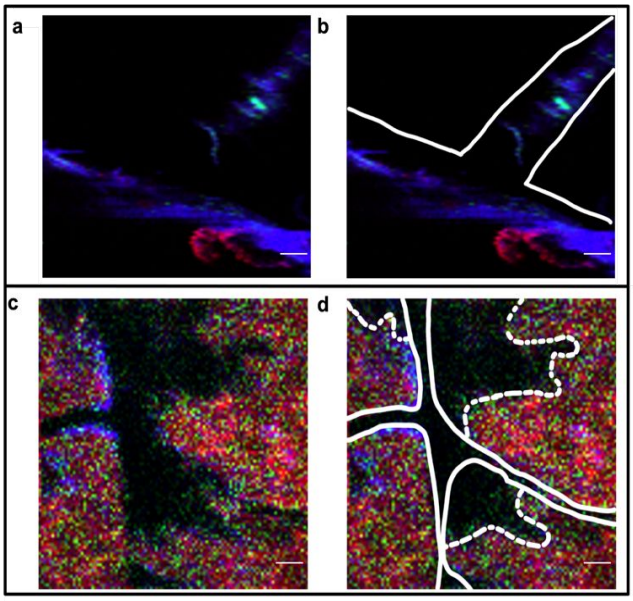

Fig. 5. (a and c) XRF confocal images of sections of the leaf treated with AuNR@Ag. (b and d) White lines have been drawn over the XRF image to delineate the veins (b) and cells (d) and demonstrate elevated concentrations of Mn (red), Zn (blue), and Au (green) within the borders of the leaf veins (b) and cells (d). The dashed white lines in (d) delineate the transition between internal and external regions of the cells within the planes of the XRF confocal image and, thus, AuNR@Ag both within and outside of the cells. Scale bar is 20 microns.

We used XRF confocal microscopy to image a 200x200 microns area within two leaves, which are shown in Fig. 5. Images were visualized and analyzed using the FIJI system.[63] The first image plane (Fig. 5a and 5b) captures vein regions of a leaf. Elevated concentrations of Mn (red) and Zn (blue) are observed throughout the leaf veins. Localized elevated Au concentration (green) are observed in parts of the vein. This is consistent with the 2D XRF image results (Fig. 4) that indicated more uniform and elevated concentrations of Mn and Zn within the veins relative to other regions of the leaf and less uniform but elevated concentrations of Au within the leaf veins. The second image plane (Fig. 5c & 5d) captures the cross-sections of 4 intact cells deeper within the leaf tissue and with different morphologies than surface pavement cells. Here, elevated concentrations of Mn (red), Zn (blue), and Au (green) define the morphology of the leaf cells and indicate that the nanorods are located predominantly inside of the leaf cells consistent with the prior TEM and confocal imaging analysis. White lines have been drawn over the XRF confocal images (Fig. 5b and 5d) to help identify the leaf veins and cells. Dashed white lines in Fig. 5d delineate the edge between internal and external regions of the cells within the plane of the XRF confocal image. Analysis of Figure 5d indicates the areas representing inside, outside, and on the cell surface to be 62%, 17%, and 21%, respectively, of the total image. Summation of pixels within Figure 5d that have Au XRF signals above background within the areas representing inside, outside, and on the cell surface were determined to be 71%, 6%, and 23%, respectively. These results indicate a greater portion of Au nanorods within the cell than outside of the cells compared to what would result from a random distribution of the Au nanorods.The ability of the AuNR@Ag to be taken up by plant cells and the Au concentration within the leaf to be measured using XRF[60, 61] enables future quantification of gold content to normalize sensor response in biological sensing measurements. It is noteworthy that 2x2x2 micron^3 voxel resolution of the confocal XRF imaging is capable of delineating individual cells that are ~100-microns in size, as illustrated in Figure 5.

2.3 In vivo Imaging and SERS Detection of Functionalized Silver-coated Gold Nanorods

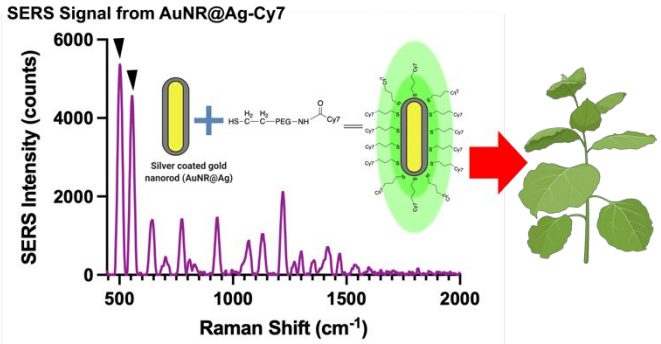

Fig 6. (a) SERS signal generated from AuNR@Ag labelled with Cy7 dye.

The first step in enabling sensing of biomolecules is ensuring the SERS spectra can be acquired inside of leaf tissued treated with AuNR@Ag conjugated with dyes. The AuNR@Ag were functionalized with a Cyanine 7 dye (Cy7-PEG-SH) and following incubation with the dye (2 µM), SERS measurements were performed on the AuNR@Ag-Cy7.

In Fig. 6, the black arrows in the spectra show the characteristic peaks of AuNR@Ag-Cy7 at 505 cm^{-1} and 558 cm^{-1}. These results demonstrate that the AuNR@Ag is an effective SERS nanoprobe under illumination with a 785-nm laser. The plasmonic properties and silver coating of

the AuNR@Ag facilitate functionalization with SERS active dyes that are superior to their gold precursor. This cell penetrating nanomaterial is unique with strong, plasmonic properties further highlighting its capability in nanosensing of intracellular biomarkers.

The two-photon cross section properties of the AuNR@Ag were also explored. The TPL excitation wavelength of AuNR@Ag was found to be at 800 nm with maximum emission at 500-600nm. For each TPL mapping, volumetric data was obtained, and the maximum amplitude projection (MAP) was displayed as the final 2D mapping image. A partially infiltrated leaf section was scanned with TPL to show the difference in TPL intensity between infiltrated and non-infiltrated leaf sections (Fig. 7b). Within the 2D profile in Fig. 7C the average pixel intensity in infiltrated sections of leaf was 128.4±78.8, ~600 times higher than the average pixel intensity in non-infiltrated sections of 0.214±0.441. This demonstrates the high TPL cross section of AuNR@Ag (Fig. 7b, c). Although fluorescent dyes can also be excited with TPL, the contrast obtained here is due to plasmonic AuNR@Ag, not Cy7 conjugated to the nanoparticle. Since emission was collected in the 500-600nm range, which is well outside of the Cy7 emission centred at 779nm, the TPL signal originates from plasmonic AuNR@Ag, not from Cy7 fluorescence. TPL is advantageous due to the high cross section of AuNR@Ag as well as high resolution in x, y, and z planes. TPL of bare AuNR@Ag without any dye coating were found to also have similar high intensity (see Fig. S8).

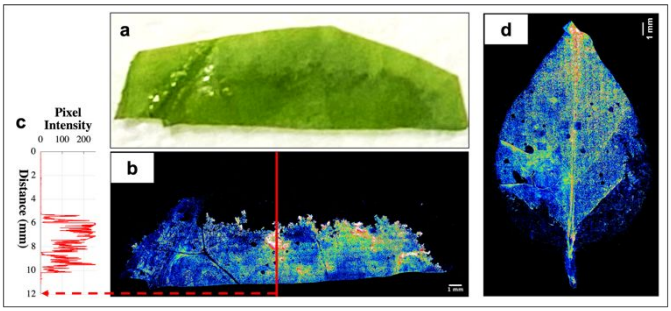

Fig. 7. (a) Image of partially infiltrated leaf section cut for imaging. Darker areas denote AuNR@Ag infiltrated sections and lighter areas show non-infiltrated sections. (b) TPL image of leaf section. Red line shows location of 2D profile plot of pixel intensities shown in (c). (d) TPL image of whole leaf treated with AuNR@Ag-Cy7.

Biological processes inside plants are dynamic events, and it is necessary to track these events with adequate spatial and temporal resolution in real time. Due to their improved plasmonic properties over those of naked gold nanorods, AuNR@Ag are versatile nanosensors that can be monitored through various optical mechanisms (PAI, TPL, XRF, Raman mapping), making them ideal SERS probes for plant monitoring applications. We exploited the combined benefits of different complementary and orthogonal imaging technologies (SERS, TPL, and PAI) to localize the infiltrated area of the AuNR@Ag. Freshly prepared AuNR@Ag functionalized with Cy7 were infiltrated into a live tobacco leaf using the needleless infiltration method as previously described. An ultrasound (US) image of the leaf was taken to aid in measurements. Two-photon imaging, photoacoustic imaging, and Raman mapping was performed on the same leaf. Because of the strong two-photon cross section intensity of the AuNR@Ag shown in Fig. 7, AuNR@Ag-Cy7 was mapped in a section of the leaf using TPL and shown in Fig. 8A. This figure shows strong TPL signal from the AuNR@Ag-Cy7, agreeing with previous measurements.

Fig. 8B shows a US image of the tobacco leaf overlaid with a (photoacoustic computed tomography) PACT image acquired at 690 nm. Both the US image and PACT image acquired volumetric data, and the maximum amplitude projection images can be extracted. The PACT overlay displays only the top 20% of normalized MAP pixels, showing strong optical absorption of AuNR@Ag at 690nm. A section of the same infiltrated leaf was also irradiated with 785-nm laser excitation, and a Raman microscope was used to collect the SERS signal as shown in Fig. 8C. The characteristic peaks of Cy7 in the spectrum of Fig. 8D provide evidence that the SERS signal is successfully collected from the decorated AuNR@Ag-Cy7 which from prior experiments have been determined to accumulate inside the plant cells. Characteristic peaks are only observable where the particles are present and not in non-infiltrated plant tissue. Moreover, characteristic peaks are not observed in the SERS spectra of a non-infiltrated plant leaf section. (see Fig. S9). The successful acquisition of spectra and the ability to identify unique Raman peaks indicates the feasibility of using the AuNR@Ag as a biosensor for sensing of RNAs, proteins, and other biomolecules. The whole leaf was not imaged using TPL and Raman mapping contributing to the incongruity of maximum signal intensities of the AuNR@Ag. This is the first recorded proof-of-concept demonstration of SERS, TPL, and PAI signal acquisition inside of living tobacco tissue using intracellular plasmonic nanosensors *in vivo.*

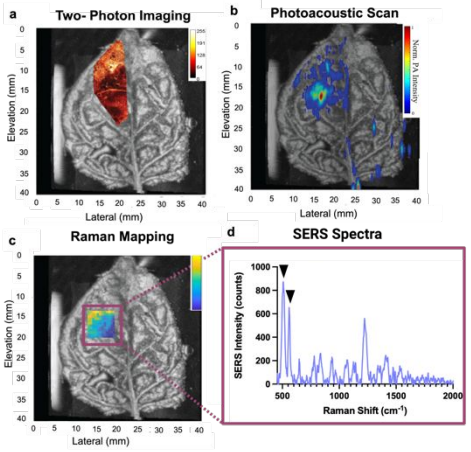

Precise future application of these techniques with other whole leaf sections has the potential to provide nanosensing with further temporal and spatial resolution. These results establish the AuNR@Ag as a novel nanotool

Fig. 8. In vivo, Multimodal Mapping of Nanorods Inside a Leaf (a) Two-photon luminescence imaging of area infiltrated with AuNR@Ag-Cy7 co-registered over ultrasound image of the leaf (b) PACT scan of the entire leaf indicating the distribution of AuNR@Ag-Cy7 (c) Raman scans of an area of the whole leaf with high intensity pixels originating from the AuNR@Ag-Cy 7. Scale bar is 0-800 counts. (d) SERS spectra from the Raman scanning of the same leaf sample.

for the study of intracellular pathways and biomolecule sensing to increase biomass development for renewable energy purposes.

Applying the different imaging techniques in Fig. 8 provides the feasibility and first demonstration of multimodal imaging using the AuNR@Ag optical bioprobes within living whole tobacco leaves with enhanced spatial and temporal resolution (see Supplementary Note 1 & 2). Having appropriate information of spatial and temporal resolution permits the understanding of regulation of many biological pathways. Research using nanoprobes within *in vivo* models have shown that particle distribution is not isotropic. Thus, normalizing nanosensor response to the number of nanosensors in each pixel via *in vivo* imaging (TPL, XRF, & PAI) can been utilized for accurate and quantitative measurements of biomarkers. In effect, imaging using XRF and plasmonics-based TPL combined with SERS biosensing achieves normalized and quantitative biomarker information. Prior work demonstrated the study of microRNA in between cells using nanostar probes with unmet spatial and temporal resolution using TPL, photoacoustic, and XRF imaging.[56] Here we have applied these techniques to a novel nanoparticle capable of entering intracellular spaces. The combination of imaging techniques will allow for calculation of probe concentration per pixel and SERS signal normalization to gold. In turn this technique can be applied to aid in the discovery of upregulated and downregulated biomarkers such as microRNA or proteins due to its unique capability to enter plant cells and enhanced plasmonic properties that permit for facile and multimodal optical imaging, localization, and quantification.

3. Conclusion

This work is the first application of a bimetallic and plasmonic nanoplatform for tobacco plant cell infiltration and sensing. The developed nanoplatform has unique characteristics that make it capable for in vivo SERS analysis: cell infiltration, plasmonic properties in the NIR, and strong SERS enhancement. The demonstration of SERS-based nanoparticles entering plant cells is a unique and important feature of this study and contribution to the field. In this work, we demonstrated how the properties of this nanoplatform can be used for SERS sensing of biological processes *in vivo*, which will permit gaining new insights for the advancement of bioenergy research. Although, we have previously designed a nanostar-based sensor for microRNA sensing in the extracellular space between plant cells[56], our previous work has not demonstrated actual internalization of the nanoprobe inside of plant cells; therefore, the demonstration of a bimetallic nanoparticle inside of plant cells is a key finding of this study and in the field.

The combination of bimetallic nanoprobe uptake and acquisition of SERS signal in leaf tissue is novel, and the combination has not been demonstrated. We designed and successfully synthesized a silver-coated nanorod with one dimension smaller than the plant cell wall exclusion size limits (5-20 nm). Using a multimodal approach combining TEM, confocal microscopy, and XRF imaging we demonstrated that AuNR@Ag nanoparticles accumulate inside of plant cells. Moreover, we demonstrated that the AuNR@Ag can be imaged and localized using a combination of optical techniques (SERS, TPL, and PAI). This is the first application of TPL and PAI of AuNR@Ag within plant tissue. These modalities further combined with SERS and XRF will allow quantification of nanosensors in other biosensing measurements. The two-photon cross-section properties of the AuNR@Ag were also explored, and it was determined that AuNR@Ag has a strong TPL cross section—the first demonstration of its kind. TPL, PAI, and XRF visualization, of the AuNR@Ag signal reveal the nanosensor's potential for the detection and quantification of biotargets through mapping and sensing. We have demonstrated the feasibility of the AuNR@Ag bioprobe as an exogenous contrast agent for PACT. AuNR@Ag is a promising candidate for contrast enhanced PAI with far-reaching potential applications in agriculture, bioenergy, and metabolic pathway monitoring. Since SERS signals are sharp and unique, they can be used for multiplex sensing, and a future AuNR@Ag biosensor has the capability for detection of multiple intracellular plant targets (RNA, DNA, protein, etc.) underscoring its ability to present novel information about intracellular biochemical pathways. Information acquired from the use of the AuNR@Ag in such intracellular pathways has the potential to revolutionize plant bioenergy and biomass production.

4. Experimental section

4.1 Chemicals and Materials

Formaldehyde, glutaraldehyde, OsO4, uranyl acetate, ERL 4221, NSA, DER 736, 2-dimethylaminoethanol (DMAE), propylene oxide, and lead citrate were all purchased from Electron Microscopy Sciences (Hatfield, PA). L(+)-ascorbic acid (AA) crystalline, polyvinylpyrrolidone (PVP, MW 25,000), silver nitrate ($AgNO_3$, 99.9999%), thiol PEG (MW 5000), ethanol, phosphate buffered saline, and sodium hydroxide were supplied by Sigma-Aldrich (St. Louis, MO). Cy7.0 PEG Thiol (Cy7.5-PEG-SH, MW 1000) were acquired from Nanocs (New York, NY). Finder copper TEM grids and 1 mL disposable syringes were obtained from VWR (Radnor, PA). All chemicals were bought at reagent grade standard. Gold nanorods capped with citrate and suspended in DI water were supplied by Nanopartz (A12-5-808-CIT-DIH-1-100). Aqua regia was used to clean all glassware and stir bars utilized in the preparation of solutions. Ultrapure water (18 MΩ·cm) was used in all synthesis and solutions. Figs. (1,3,6,8), supplementary fig. 12, and supplementary schematic 1 were created in part using BioRender.

4.2 Silver Coating of Gold Nanorods

Silver coating of the nanorods was adapted from a previously described synthesis.[60] Briefly, gold nanorods as received (8 mL) were sonicated for 5 minutes, and then added to 20 mL of a 2% PVP solution under moderate stirring in a flat round bottom flask. An aliquot (0.75 mL,1 mM) of $AgNO_3$ was added to the solution, followed by the quick addition of ascorbic acid (0.5 mL, 0.1 M). After the mixture was stirred for 2 minutes, NaOH (1 mL, 0.1 M) was added, and the solution was stirred for an additional 2 minutes. The solution turned from light brown to green at the end of the synthesis. The AuNR@Ag were centrifuged and washed at 14000 g after incubating at room temperature for 2 hrs. The silver-coated nanorods were used for experiments and characterized following centrifugation and resuspension in ultrapure water. For SERS, TEM, TPL, XRF, and PAI experiments, the AuNR@Ag were concentrated to 800 µL. For confocal imaging, the AuNR@Ag were concentrated to 80 µL. For SERS imaging and sensing, the AuNR@Ag were incubated with Cy7-PEG-SH (2 µM, 1000 MW) for 1hr, and then incubated with mPEG-SH (2 µM, 5000 MW) for stability for 1 hr at room temperature. After the incubation, the AuNR@Ag were centrifuged, washed, and resuspended in Millipore water as stated above. For confocal experiments, Cy3-PEG-SH (1000 MW, 1 µM) was added to the AuNR@Ag and permitted to incubate for 1 hr. After addition of the cyanine dye, mPEG-SH (5000 MW, 1 µM) was added for a 1 hr incubation time period at room temperature. All AuNR@Ag solutions were sonicated for 2 minutes prior to measurements or injection into the leaves. Zeta potential measurements were performed with a Zetasizer Nano ZS instrument (Malvern Analytical) using a zeta potential cuvette.

4.3 Procedure for Plant Growth and Materials

The p35S-HA-GFP plasmid was constructed using binary vector pGFC5941 and the plasmid pSMGFP containing the GFP gene (ABRC stock numbers CD-447 and CD3-326, respectively). The HA-tag was generated by annealing the primers HA-tag-F (5'-CATGGCGTACCCGTACGACGTGCCCGACTACGCCAG) and HA-tag-R (5'-GATCCTGGCGTAGTCGGGCACGTCGTACGGGTACGC) that create NcoI and BamHI sticky ends. The plasmid pGFC5941 was digested with NcoI and XbaI to remove the RNAi cassette. Then, the synthetic HA-tag and the full-length GFP gene flanked by BamHI and XbaI ends were cloned into the NcoI/XbaI sites of pGFC5941 rendering an N-terminal HA-tagged GFP protein driven by the 35S promoter. The p35S-HA-GFP plasmid was then transformed to Agrobacterium strain GV3101. For tobacco transient expression, leaves of four-week-old tobacco (*Nicotiana benthamiana*) plant were infiltrated using agrobacteria containing p35S-HA-GFP, following procedures described previously.[64] It has been well documented that the GFP protein can be localized to both cytoplasm and nucleus when expressed in plant cells.[65] GFP lacks any transmembrane sequence and is not targeted to cell membranes. This protein also lacks nuclear localization signal, which facilitates protein translocation into the nucleus. However, GFP is known to be also present in the nucleus because of its small size (27 kD).

4.4 Needleless Infiltration of Tobacco Leaves

Two days after p35S-HA-GFP infiltration, tobacco leaves were infiltrated with nanoprobes via needleless injection on the abaxial side of the leaf, as previously described.[56] In brief, a 1 mL micropipette tip was gently pressed on the abaxial side of the leaf. Over the center of the indentation, a 1 mL syringe without a needle was used to inject the leaf with AuNR@Ag. The leaves were carefully rinsed with deionized water to remove surface particles and maintained in a humid environment prior to measurements. Confocal, TEM, SERS, TPL, and photoacoustic measurements of the nanorods infiltrated into the leaf were performed 0.5-4 hours after infiltration. Following confocal imaging, leaves were maintained hydrated and prior to shipping, encased in Kapton Tape and placed in a petri dish secured with parafilm.

4.5 Dimension Characterization of Particles

The nanorod TEM images were processed using the ImageJ software to create and quickly analyze the average characteristics of each nanorod particle. To limit user bias, an image processing pipeline was used to process the TEM images sequentially. [66, 67] The image was first denoised by gaussian filtering to reduce image specks. Next, the Otsu thresholding algorithm was used to roughly demarcate the boundaries of each particle, and the resulting images were then filtered to remove recorded objects whose area were greater than 100 nm^2 and less than 600 nm^2 with the assumption that these objects were either noise or particle aggregates and thus should be ignored. The resulting detected objects were then run through the Analyze Particles function to obtain the length (Ferret diameter) and width (minimum Ferret diameter). The ratio of these two values were used to calculate the aspect ratio of the nanoparticle. Fig. S2 details the pipeline workflow as described above. Fig. S3 and supplementary Table 1 show that the silver-coated gold nanorods have an average width of 13 nm.

4.6 TEM Sample Preparation and Imaging

After the leaves were treated with nanoparticles, the infiltrated section was cut and overlaid with fixative containing formaldehyde and glutaraldehyde. After being in fixative for two days and washed with PBS, they were placed in OsO_4. After incubation in OsO_4, the leaf samples were washed in a series of buffers and stained with uranyl acetate. Following staining, they were washed in increasing amounts of ethanol and placed in propylene oxide. A mixture of resin (ERL 4221, NSA, and DER 736) was added with DMAE to the samples. Samples were placed in wells and the resin was allowed to harden in an oven for two days. Once the samples hardened in the oven, they

were sliced using a microtome and laid on transmission electron microscopy (TEM) grids. Grids were counterstained with uranyl acetate and lead citrate. TEM micrographs were acquired using a FEI Tecnai G2 twin transmission electron microscope at 120 kV.

4.7 Confocal Imaging Methods

To test for nanoparticle infiltration, confocal microscopy imaging was utilized to observe and analyze colocalization of Cy3 fluorophore tagged nanoparticles inside tobacco leaves expressing green fluorescent protein (GFP) in the cytoplasm. AuNR@Ag probes with Cy3 were introduced into the leaves by pressing a needleless syringe loaded with labelled nanoparticles to the abaxial side of the leaf. Leaves were permitted to incubated for 3 hours with tagged nanoparticles before imaging with a Zeiss 880 Airy Scan Confocal Microscope. A 488 nm laser was used to excite the GFP channel, and a 561 nm was used to excite the Cy3 channel. The image size was 425.1 x 425.1 µm. Images were processed using FIJI. Mander's overlap coefficients were calculated from the averages of Z-projected images of 3 separate leaf samples and 5 different fields of view in each leaf. Fig. S10 shows images of leaves not treated with AuNR@Ag-Cy3 and non-GFP transformed plants treated with particles.

4.8 XRF Elemental Mapping of Leaves treated with AuNR@Ag

Synchrotron x-ray fluorescence (XRF) elemental mapping[68, 69] was carried out at the MR-CAT/EnviroCAT insertion device beamline (Sector 10-ID) at the Advanced Photon Source (APS).[70] The energy of the probe x-ray beam was set at 12,000 eV, which is above the Au L_{III} absorption edge and thus able to excite the L_{III} x-ray fluorescence lines of the Au atoms in the sample. The emitted fluorescence was collected and analyzed with a 4-element Si detector (Vortex) set at 90 degrees horizontally relative to the incident beam. The Multi-Channel Analyzer (MCA) electronics were calibrated to the fluorescence energies of Cu, Co, Mn, V, and Ca using a NIST 1832 standard. The imaging measurement was performed with a 10 µm (horizontally defined by slits) by 14 µm (vertically focused by a bent Rh mirror) beam, producing approximately a 14x14µm spot on the sample that was set at 45 degrees relative to the beam in the horizontal direction. Samples were raster scanned in front of the beam in 10h x 10v micron steps. The x-axes of the XRF maps were corrected for the 45-degree angle of the sample by scaling the sample stage positions by 1.414. The XRF energy regions of interest used for the maps were defined based on the expected elemental content of biological samples and the additional lines observed in the XRF spectra of the samples, including the following elements: Au, P, S, Cl, Ca, Mn, Fe, Ni, Cu, Zn.

4.9 XRF Confocal Imaging

Because the x-ray probe used in conventional 2D XRF imaging passes through the plant leaf, the elemental content contained through the thickness of a leaf is integrated into a 2D elemental image. Confocal XRF (CXRF) microscopy allows spatial discrimination of XRF photons from a sample in all three dimensions.[71] CXRF employs overlapping focal regions of two x-ray optics—a condenser and collector—to directly probe a 3D volume in space. Although polycapillaries are the most common collection optics used for CXRF microscopy, they limit the technique to depth resolution of 10s of microns. In contrast to polycapillaries, recently developed Collimating Channel Arrays (CCAs) provide both an overall improvement in resolution and, importantly, spatial resolution that is invariant with the x-ray fluorescence energy.[72] The new CXRF microscopy capability at sector 20-ID at the APS, enabled by CCAs, are capable of achieving depth resolution of 2 µm. In addition, CXRF microscopy significantly improves the signal-to-noise ratio by rejecting background scattering, thus increasing the limit of detection of fluorescent x-rays.

CXRF experiments measurements making use of CCAs were made at the 20-ID beamline of the APS [72-74] on the same three samples that were previously measured with 2D XRF at the MRCAT/EnviroCAT beam line at the APS. An incident x-ray energy of 12keV was used for the measurements. Samples were placed at 35 degrees relative to the incident x-ray beam. A single element SDD Vortex detector was placed at 90 degrees relative to the beam on the opposite side of the samples. A 2-micron resolution CCA was used with the SDD detector. The incoming X-ray beam was focused with profile coated KB mirrors, creating a focal spot of 2 microns in diameter. Samples were measured under ambient conditions. XRF maps (200x200 microns) were collected by rastering the samples through a 2x2x2 microns confocal volume with 400ms dwell time per pixel, followed by movement of the sample by 2 microns to a new depth for measurement of a subsequent 200x200 microns XRF map.

4.10 Two-Photon Luminescence of Silver-coated Au Nanorods in Tobacco Leaf

Infiltrated leaf sections were cut and secured between a petri dish and coverslip, fastened with tape, immersed with DI, and imaged under the Leica SP8 2photon DIVE. Multiphoton images were obtained under 25X/1.05 NA objective with 800 nm two photon excitation from Ti:Saph laser at 3.5% laser intensity, 80 MHz rep rate, and 140 fs pulse width. Photons were detected in the 500-600nm range. Field of view was scanned by automated XY motorized stage with pixel dwell time of 13.85us and frame rate: 2.17/s. A z-stack of 5 was obtained with z-step size of ~60µm to capture signal in the entire leaf. Max projection of z-stack was calculated in FIJI. Scale bar is 1mm.

4.11 Photoacoustic Imaging

Method: In photoacoustic imaging (PAI), a sample is illuminated with a short laser pulse, causing the excited molecular absorbers within the sample to heat up and undergo thermoelastic expansion. This expansion results in a broadband ultrasound wave propagating out from the excited target, thus allowing for ultrasound detection and subsequently image reconstruction[75]. This imaging mechanism allows PAI to be a modality that combines optical contrast with acoustic resolution. PAI is a highly scalable imaging modality, thus there exists two major subdivisions: photoacoustic microscopy (PAM) and photoacoustic computed tomography (PACT)[76]. PAM can achieve a micrometer-level spatial resolution at a millimeter-level imaging depth, while PACT can achieve submillimeter spatial resolutions with imaging depths on the order of centimeters. Due to this high scalability, PAI systems are used in subcellular, cellular, tissue, and organ imaging applications. PAI often utilizes endogenous biomolecules (e.g., hemoglobin, lipids, melanin). There exists great interest in the study of exogenous contrast agents for PAI because they can provide high molecular specificity [77-79].

System: A photoacoustic computed tomography (PACT) system was used to detect AuNR@Ag infiltration, along with co-registered 50MHz ultrasound (US) imaging to provide structural information. The PACT system includes a linear-array transducer (L7-4, Philips, USA) bilaterally coupled with line fiber-bundles for wide-field laser excitation. An Nd:YAG laser (Q-smart 850, Quantel Laser, USA) (532 nm) was used to pump an optical parametric oscillator (OPO) (versaScan-L532, Spectral Physics, USA). The US imaging system uses a fixed-focus dual-element wobbler ultrasound transducer. Both transducers are submerged in oil for acoustic coupling and include an imaging window on which the samples are placed (Fig. S7). The tobacco leaf, treated with AuNR@Ag-Cy7 and bare AuNR@Ag, was inserted between two 5mm-thick slabs of agar, along with a layer of water for acoustic coupling, and placed on the imaging window. A US image was first acquired using the wobbler transducer, followed by the PACT scan. The OPO laser provided light at 680 nm, 750 nm, and 1064 nm which were used to excite the tobacco leaf for PACT imaging (Fig. S11). The PACT volumes were acquired by averaging 10 frames per elevational position and scanning the transducer with an elevational step size of 0.2 mm.

4.12 Optical Configuration for Raman Mapping

A laboratory-built Raman microscope was used for the Raman mapping measurements. The setup consists of an inverted microscope (Ti-U; Nikon Instruments Inc., Melville, NY) with an excitation source laser at a wavelength 785 nm diode laser with a power of 300 mW (Optoengine Midvale, UT). The laser is then focused into the image plane of the microscope objective (laser spot = 500 µm). The microscope is equipped with a filter cube containing a laser line filter, dichroic mirror, and a notch filter fit for the 785 nm excitation light (Semrock, Rochester, NY). To visualize the whole leaf, an objective of NA=0.1 from Thorlabs, Newton, NJ was used. The stage movements (100 mm x 120 mm travel RS-232; Zaber, Vancouver, CA) and spectra acquisition were coordinated using a LabVIEW code (National Instruments, Austin, TX). A spatial resolution of 500µm and spot size of 500µm were used to capture the Raman images.

The Raman spectra of the AuNR@Ag were collected using a spectrometer (1200 grooves mm−1 grating) coupled to a CCD camera (LS785 and Pixis100; Princeton Instruments, Trenton, NJ). A circular-to-linear fiber optic bundle (Thorlabs, Newton, NJ) connected the camera to the microscope. Fig. S12 renders a schematic representation of the lab-built Raman microscope setup described above. The background subtraction and smoothing of the spectra was performed on Matlab using a Savitzky–Golay filter (five-point window and first-order polynomial). For the SERS Cy7 tags on the AuNR@Ag, 1 accumulation each of 3s were used.

Author Contributions

The manuscript and work were executed by all contributions of the authors. Every author has revised and given approval to the submitted manuscript. Author VCG synthesized and characterized the AuNR@Ag; she also acquired the confocal, TEM, and SERS images. VCG wrote the manuscript, coordinated the experiments, and lead the project. Author JQL developed the TPL method and acquired the TPL images. Author SJN assisted with calculations. RAO performed the sizing analysis. PS advised on the synthetic strategy and scope of the project. LM, CM, and JY performed the PAI. JH, RZ, and TS provided all the modified and native tobacco plants. MIB, YZF, DG, DSD, and KMK acquired and analyzed the XRF data, and corresponding optical images. TV supervised and guided the project.

Conflicts of interest

All the authors declare no conflict of interests related to the work presented in the manuscript.

Acknowledgements

This work was funded by US Department of Energy Offices of Science, under Award Number (DE-SC0019393). The Advanced Photon Source, a U. S. Department of Energy (DOE) Office of Science User Facility operated for the DOE Office of Science by Argonne National Laboratory under Contract No. DE-AC02-06CH11357 and the Canadian Light Source and its funding partners helped in the acquisition of the data in this research. The DOE and MRCAT/EnviroCAT member institutions support the MRCAT/EnviroCAT

operations. We kindly thank the MRCAT beamline staff for their time and efforts during 2D XRF elemental mapping data collection at the MRCAT/EnviroCAT. The TEM imaging and UV-vis spectroscopy in this work were performed in part at the Duke University Shared Materials Instrumentation Facility (SMIF), a member of the North Carolina Research Triangle Nanotechnology Network (RTNN), which is supported by the National Science Foundation (award number ECCS-2025064) as part of the National Nanotechnology Coordinated Infrastructure (NNCI). The researcher Joy Li acknowledges and thanks the support provided by the NDSEG Fellowship (Fellow ID: 00007902). Vanessa Cupil-Garcia thanks the funding and support provided by the Fitzpatrick Foundation Scholars Award.

Notes

Corresponding Author

*Author for correspondence is Dr. Tuan Vo-Dinh (tuan.vodinh@duke.edu).

Present Author Addresses:

1. Department of Chemistry, University of Cincinnati 2600 Clifton Ave, Cincinnati, OH 45221, USA

2. U.S. Department of Agriculture, Agricultural Research Service, Plant Science Research Unit, Raleigh, NC 27607, USA

3. Department of Crop and Soil Sciences, North Carolina State University, Raleigh, NC 27695, USA

4. Illinois Institute of Technology, Chicago, IL 60616, USA

References

1. S. Kaur, L. K. Sarao, Ankita and H. Singh, in *Agroindustrial Waste for Green Fuel Application*, eds. N. Srivastava, B. Verma and P. K. Mishra, Springer Nature Singapore, Singapore, 2023, DOI: 10.1007/978-981-19-6230-1_9, pp. 281-311.
2. C.-Y. Wang, S. Zhang, Y. Yu, Y.-C. Luo, Q. Liu, C. Ju, Y.-C. Zhang, L.-H. Qu, W. J. Lucas, X. Wang and Y.-Q. Chen, *Plant Biotechnol. J.*, 2014, **12**, 1132-1142.
3. Q. Dong, B. Hu and C. Zhang, *Frontiers in Plant Science*, 2022, **13**.
4. T. Unver, D. M. Namuth-Covert and H. Budak, *Int J Plant Genomics*, 2009, **2009**, 262463.
5. P. Wang, E. Lombi, F.-J. Zhao and P. M. Kopittke, *Trends Plant Sci.*, 2016, **21**, 699-712.
6. T. Eichert, A. Kurtz, U. Steiner and H. E. Goldbach, *Physiol. Plant.*, 2008, **134**, 151-160.
7. F. J. Cunningham, N. S. Goh, G. S. Demirer, J. L. Matos and M. P. Landry, *Trends Biotechnol.*, 2018, **36**, 882-897.
8. E. Spielman-Sun, A. Avellan, G. D. Bland, R. V. Tappero, A. S. Acerbo, J. M. Unrine, J. P. Giraldo and G. V. Lowry, *Environmental Science: Nano*, 2019, **6**, 2508-2519.
9. F. Schwab, G. Zhai, M. Kern, A. Turner, J. L. Schnoor and M. R. Wiesner, *Nanotoxicology*, 2016, **10**, 257-278.
10. S. B. Gelvin, *Annu. Rev. Genet.*, 2017, **51**, 195-217.
11. M. Mahmoudi, K. Azadmanesh, M. A. Shokrgozar, W. S. Journeay and S. Laurent, *Chem. Rev.*, 2011, **111**, 3407-3432.
12. S. Behzadi, V. Serpooshan, W. Tao, M. A. Hamaly, M. Y. Alkawareek, E. C. Dreaden, D. Brown, A. M. Alkilany, O. C. Farokhzad and M. Mahmoudi, *Chem. Soc. Rev.*, 2017, **46**, 4218-4244.
13. T. Vo-Dinh, J. P. Alarie, B. M. Cullum and G. D. Griffin, *Nat. Biotechnol.*, 2000, **18**, 764-767.
14. R. M. Kasili, B. M. Cullum, G. D. Griffin and T. Vo-Dinh, *Journal of Nanoscience and Nanotechnology*, 2002, **2**, 653-658.
15. P. M. Kasili and T. Vo-Dinh, *Polycyclic Aromatic Compounds*, 2004, **24**, 221-235.
16. P. M. Kasili and T. Vo-Dinh, *Journal of Nanoscience and Nanotechnology*, 2005, **5**, 2057-2062.
17. J. P. Scaffidi, M. K. Gregas, V. Seewaldt and T. Vo-Dinh, *Anal. Bioanal. Chem.*, 2009, **393**, 1135-1141.
18. B. M. Crawford, R. L. Shammas, A. M. Fales, D. A. Brown, S. T. Hollenbeck, T. Vo-Dinh and G. R. Devi, *International Journal of Nanomedicine*, 2017, **12**, 6259-6272.
19. E. C. Wang and A. Z. Wang, *Integrative biology : quantitative biosciences from nano to macro*, 2014, **6**, 9-26.
20. R. Mout, M. Ray, G. Yesilbag Tonga, Y.-W. Lee, T. Tay, K. Sasaki and V. M. Rotello, *ACS Nano*, 2017, **11**, 2452-2458.
21. E. E. Connor, J. Mwamuka, A. Gole, C. J. Murphy and M. D. Wyatt, *Small*, 2005, **1**, 325-327.
22. E. Navarro-Palomares, L. García-Hevia, J. Galán-Vidal, A. Gandarillas, F. García-Reija, A. Sánchez-Iglesias, L. Liz-Marzán, R. Valiente and M. Fanarraga, *Journal*, 2022, DOI: 10.21203/rs.3.rs-1640813/v1.
23. T. D. Payne, S. J. Klawa, T. Jian, S. H. Kim, M. J. Papanikolas, R. Freeman and Z. D. Schultz, *ACS Sens*, 2021, **6**, 3436-3444.
24. X. Gu, H. Wang, Z. D. Schultz and J. P. Camden, *Anal. Chem.*, 2016, **88**, 7191-7197.
25. C. Lima, S. Ahmed, Y. Xu, H. Muhamadali, C. Parry, R. J. McGalliard, E. D. Carrol and R. Goodacre, *Chemical Science*, 2022, **13**, 8171-8179.
26. R. K. Kannadorai, G. G. Y. Chiew, K. Q. Luo and Q. Liu, *Cancer Lett.*, 2015, **357**, 152-159.
27. I. Sanzari, A. Leone and A. Ambrosone, *Frontiers in bioengineering and biotechnology*, 2019, **7**, 120-120.
28. A. Albanese, P. S. Tang and W. C. W. Chan, *Annu. Rev. Biomed. Eng.*, 2012, **14**, 1-16.
29. F. Torney, B. G. Trewyn, V. S. Y. Lin and K. Wang, *Nature Nanotechnology*, 2007, **2**, 295-300.
30. Z.-J. Zhu, H. Wang, B. Yan, H. Zheng, Y. Jiang, O. R. Miranda, V. M. Rotello, B. Xing and R. W. Vachet, *Environ. Sci. Technol.*, 2012, **46**, 12391-12398.
31. T. Sabo-Attwood, J. M. Unrine, J. W. Stone, C. J. Murphy, S. Ghoshroy, D. Blom, P. M. Bertsch and L. A. Newman, *Nanotoxicology*, 2012, **6**, 353-360.
32. J. M. Buriak, L. M. Liz-Marzán, W. J. Parak and X. Chen, *ACS Nano*, 2022, **16**, 1681-1684.

33. Y. Su, V. E. T. M. Ashworth, N. K. Geitner, M. R. Wiesner, N. Ginnan, P. Rolshausen, C. Roper and D. Jassby, *ACS Nano*, 2020, **14**, 2966-2981.
34. C.-W. Yang, Y. Hu, L. Yuan, H.-Z. Zhou and G.-P. Sheng, *ACS Nano*, 2021, **15**, 19828-19837.
35. G. S. Demirer, H. Zhang, J. L. Matos, N. S. Goh, F. J. Cunningham, Y. Sung, R. Chang, A. J. Aditham, L. Chio, M.-J. Cho, B. Staskawicz and M. P. Landry, *Nature Nanotechnology*, 2019, **14**, 456-464.
36. A. Avellan, J. Yun, Y. Zhang, E. Spielman-Sun, J. M. Unrine, J. Thieme, J. Li, E. Lombi, G. Bland and G. V. Lowry, *ACS Nano*, 2019, **13**, 5291-5305.
37. A. Avellan, F. Schwab, A. Masion, P. Chaurand, D. Borschneck, V. Vidal, J. Rose, C. Santaella and C. Levard, *Environ. Sci. Technol.*, 2017, **51**, 8682-8691.
38. S. Martin-Ortigosa, J. S. Valenstein, W. Sun, L. Moeller, N. Fang, B. G. Trewyn, V. S. Y. Lin and K. Wang, *Small*, 2012, **8**, 413-422.
39. Y. Hao, X. Yang, Y. Shi, S. Song, J. Xing, J. Marowitch, J. Chen and J. Chen, *Botany*, 2013, **91**, 457-466.
40. H. Zhang, Y. Cao, D. Xu, N. S. Goh, G. S. Demirer, S. Cestellos-Blanco, Y. Chen, M. P. Landry and P. Yang, *Nano Lett.*, 2021, **21**, 5859-5866.
41. H. Zhang, N. S. Goh, J. W. Wang, R. L. Pinals, E. González-Grandío, G. S. Demirer, S. Butrus, S. C. Fakra, A. Del Rio Flores, R. Zhai, B. Zhao, S.-J. Park and M. P. Landry, *Nature Nanotechnology*, 2021, DOI: 10.1038/s41565-021-01018-8.
42. M. Fleischmann, P. J. Hendra and A. J. McQuillan, *Chem. Phys. Lett.*, 1974, **26**, 163-166.
43. D. L. Jeanmaire and R. P. Van Duyne, *J. Electroanal. Chem.*, 1977, **84**, 1-20.
44. M. G. Albrecht and J. A. Creighton, *JACS*, 1977, **99**, 5215-5217.
45. M. R. Philpott, *The Journal of Chemical Physics*, 1975, **62**, 1812-1817.
46. M. Moskovits, *The Journal of Chemical Physics*, 1978, **69**, 4159-4161.
47. J. Langer, D. J. de Aberasturi, J. Aizpurua, R. A. Alvarez-Puebla, B. Auguie, J. J. Baumberg, G. C. Bazan, S. E. J. Bell, A. Boisen, A. G. Brolo, J. Choo, D. Cialla-May, V. Deckert, L. Fabris, K. Faulds, F. J. G. de Abajo, R. Goodacre, D. Graham, A. J. Haes, C. L. Haynes, C. Huck, T. Itoh, M. Ka, J. Kneipp, N. A. Kotov, H. Kuang, E. C. Le Ru, H. K. Lee, J. F. Li, X. Y. Ling, S. A. Maier, T. Mayerhofer, M. Moskovits, K. Murakoshi, J. M. Nam, S. Nie, Y. Ozaki, I. Pastoriza-Santos, J. Perez-Juste, J. Popp, A. Pucci, S. Reich, B. Ren, G. C. Schatz, T. Shegai, S. Schlucker, L. L. Tay, K. G. Thomas, Z. Q. Tian, R. P. Van Duyne, T. Vo-Dinh, Y. Wang, K. A. Willets, C. Xu, H. Xu, Y. Xu, Y. S. Yamamoto, B. Zhao and L. M. Liz-Marzan, *ACS Nano*, 2020, **14**, 28-117.
48. M. Boscacci, S. Francone, K. Galli and S. Bruni, *Journal of Raman Spectroscopy*, 2020, **51**, 1108-1117.
49. A. M. Fales, H. K. Yuan and T. Vo-Dinh, *J. Phys. Chem. C*, 2014, **118**, 3708-3715.
50. T. Vo-Dinh, *TrAC, Trends Anal. Chem.*, 1998, **17**, 557-582.
51. Y. Liu, Z. Chang, H. K. Yuan, A. M. Fales and T. Vo-Dinh, *Nanoscale*, 2013, **5**, 12126-12131.
52. Y. Liu, P. Maccarini, G. M. Palmer, W. Etienne, Y. Zhao, C.-T. Lee, X. Ma, B. A. Inman and T. Vo-Dinh, *Sci. Rep.*, 2017, **7**, 8606.
53. H. T. Ngo, N. Gandra, A. M. Fales, S. M. Taylor and T. Vo-Dinh, *Biosens. Bioelectron.*, 2016, **81**, 8-14.
54. V. Cupil-Garcia, P. Strobbia, B. M. Crawford, H.-N. Wang, H. Ngo, Y. Liu and T. Vo-Dinh, *Journal of Raman Spectroscopy*, 2021, **52**, 541-553.
55. S. Atta, T. Watcharawittayakul and T. Vo-Dinh, *Analyst*, 2022, **147**, 3340-3349.
56. B. M. Crawford, P. Strobbia, H. N. Wang, R. Zentella, M. I. Boyanov, Z. M. Pei, T. P. Sun, K. M. Kemner and T. Vo-Dinh, *ACS Appl. Mater. Interfaces*, 2019, **11**, 7743-7754.
57. P. Strobbia, Y. Ran, B. M. Crawford, V. Cupil-Garcia, R. Zentella, H. N. Wang, T. P. Sun and T. Vo-Dinh, *Anal. Chem.*, 2019, **91**, 6345-6352.
58. W. K. Son, Y. S. Choi, Y. W. Han, D. W. Shin, K. Min, J. Shin, M. J. Lee, H. Son, D. H. Jeong and S.-Y. Kwak, *Nature Nanotechnology*, 2023, **18**, 205-216.
59. H. Zhang, G. S. Demirer, H. Zhang, T. Ye, N. S. Goh, A. J. Aditham, F. J. Cunningham, C. Fan and M. P. Landry, *Proceedings of the National Academy of Sciences*, 2019, **116**, 7543.
60. M. Pastorello, F. A. Sigoli, D. P. Dos Santos and I. O. Mazali, *Spectrochim Acta A Mol Biomol Spectrosc*, 2020, **231**, 118113.
61. C. Zhang, G. R. Hicks and N. V. Raikhel, *Frontiers in Plant Science*, 2014, **5**.
62. K. M. Kemner, S. D. Kelly, B. Lai, J. Maser, E. J. O'Loughlin, D. Sholto-Douglas, Z. Cai, M. A. Schneegurt, C. F. Kulpa and K. H. Nealson, *Science*, 2004, **306**, 686-687.
63. J. Schindelin, I. Arganda-Carreras, E. Frise, V. Kaynig, M. Longair, T. Pietzsch, S. Preibisch, C. Rueden, S. Saalfeld, B. Schmid, J.-Y. Tinevez, D. J. White, V. Hartenstein, K. Eliceiri, P. Tomancak and A. Cardona, *Nat. Methods*, 2012, **9**, 676-682.
64. Z.-L. Zhang, M. Ogawa, M. Fleet Christine, R. Zentella, J. Hu, J.-O. Heo, J. Lim, Y. Kamiya, S. Yamaguchi and T.-p. Sun, *Proceedings of the National Academy of Sciences*, 2011, **108**, 2160-2165.
65. R. H. Kohler, *Trends Plant Sci.*, 1998, **3**, 317-320.
66. E. A. Grulke, X. Wu, Y. Ji, E. Buhr, K. Yamamoto, N. Woong Song, A. B. Stefaniak, D. Schwegler-Berry, W. W. Burchett, J. Lambert and A. J. Stromberg, *Metrologia*, 2018, **55**, 254-267.
67. S. Mehmet and S. Bülent, *Journal of Electronic Imaging*, 2004, **13**, 146-165.
68. M. I. Boyanov and K. M. Kemner, in *Analytical Geomicrobiology: A Handbook of Instrumental Techniques*, eds. D. S. Alessi, H. Veeramani and J. P. L. Kenney, Cambridge University Press, Cambridge, 2019, DOI: DOI: 10.1017/9781107707399.010, pp. 238-261.
69. K. M. Kemner and S. D. Kelly, *Manual of Environmental Microbiology, 3RD ED*, 2007, 1183-1194.
70. C. U. Segre, N. E. Leyarovska, L. D. Chapman, W. M. Lavender, P. W. Plag, A. S. King, A. J. Kropf, B. A. Bunker, K. M. Kemner, P. Dutta, R. S. Duran and J.

Kaduk, *AIP Conference Proceedings*, 2000, **521**, 419-422.
71. C. Jacobsen, *X-ray Microscopy*, Cambridge University Press, Cambridge, 2019.
72. D. N. Agyeman-Budu, S. Choudhury, I. Coulthard, R. Gordon, E. Hallin and A. R. Woll, *AIP Conference Proceedings*, 2016, **1764**, 020004.
73. S. Heald, E. Stern, D. Brewe, R. Gordon, D. Crozier, D. Jiang and J. Cross, *J Synchrotron Radiat*, 2001, **8**, 342-344.
74. S. M. Heald, J. O. Cross, D. L. Brewe, R. A. Gordon and U. Simon Frazer, United States, 2007.
75. M. Xu and L. V. Wang, *Rev. Sci. Instrum.*, 2006, **77**, 041101.
76. L. V. Wang and J. Yao, *Nat. Methods*, 2016, **13**, 627-638.
77. J. Weber, P. C. Beard and S. E. Bohndiek, *Nat. Methods*, 2016, **13**, 639-650.
78. W. Li and X. Chen, *Nanomedicine (London, England)*, 2015, **10**, 299-320.
79. X. Yang, E. W. Stein, S. Ashkenazi and L. V. Wang, *WIREs Nanomedicine and Nanobiotechnology*, 2009, **1**, 360-368.